

Figure S1. Defects in brain and spinal cord in *Epg5*^{-/-} mice. (A) The numbers of Nissl-stained neurons in cortical layers 1–4 are similar in control and *Epg5* knockout mice. Means \pm SEM of three mice are shown. (B) The box indicates the area of the fifth cortical layer that was scored for neurons shown in Fig. 2 B. (C) Anti-β-tubulin III staining of the alveus of the hippocampus shows the slightly irregular arrangement of axonal fibers in *Epg5*^{-/-} mice. (D) Axons of Purkinje cells in the DCN region, stained by anticalbindin, show no obvious difference in mutant mice. (E) EM pictures of the lumbar spinal cords from *Epg5*^{-/-} mice at 10 mo of age. Arrows indicate swollen mitochondria. (F) Compared with control mice, dying cells (arrows) accumulate in the cortex in *Epg5*^{-/-} mice. (G and H) GFAP staining of cortex (G) and Purkinje cell layer (H) shows reactive astrocytosis in *Epg5*^{-/-} mice. (I) No elevation of p62 mRNA level in *Epg5*-deficient cerebrum, cerebellum, and spinal cord (SC). The transcription levels of p62 mRNA were normalized to *actin* mRNA. Results are representative of at least three experiments. Error bars indicate SEMs. (J) Compared with control littermates, proteasome activity is not altered in brain extracts of *Epg5*^{-/-} mice at 10 mo of age. A, Ac-Gly-Pro-Leu-Asp-AMC; B, Suc-Leu-Leu-Val-Tyr-AMC; C, Ac-Arg-Leu-Arg-AMC; D, Boc-Leu-Arg-Arg-AMC. Error bars indicate SEMs. (K and L) p62 immunostaining shows that p62 aggregates accumulate in hypothalamus (K) and thalamus (L) in *Epg5*^{-/-} mice. (M) Costaining of p62 and calbindin shows p62 aggregates surrounding Purkinje cells in *Epg5*^{-/-} mice. (N) Double immunofluorescence staining of p62 (red) and ubiquitin (green) aggregates in the DCN in cerebellum of *Epg5*^{-/-} mice reveals the colocalization of p62 and ubiquitin. (O) Percentages of LC3 dots colocalized with p62 aggregates. Means \pm SEM of three mice are shown. AH, anterior horn. (P) LC3 (red) and SMI 32 (green) costaining reveals the presence of LC3 dots in motor neurons in the anterior horn of the lumbar spinal cord of *Epg5*^{-/-} mice. (Q and R) Double staining of hippocampus and anterior horn from *Epg5*^{-/-} and *Epg5*^{+/-} mice shows that LC3 dots are colocalized with p62 aggregates. (S) Total brain and spinal cord proteins from *Epg5*^{+/-} and *Epg5*^{-/-} mice were extracted, separated by SDS-PAGE, and analyzed by immunoblotting with anti-TDP-43 antibodies. Results are representative of at least three experiments. (T and U) Immunostaining with anti-TDP-43 indicates that TDP-43 aggregates accumulate in the cytoplasm of motor neurons in *Epg5*^{-/-} mice (T) but not in *Ei24*^{flox/flox}; nestin (Nes)-Cre mice (U). LC, lateral column. Bars: (B) 200 μm; (C, D, K–N, P–R, T, and U) 10 μm; (E) 2 μm; (F) 5 μm; (G) 50 μm; (H) 20 μm.

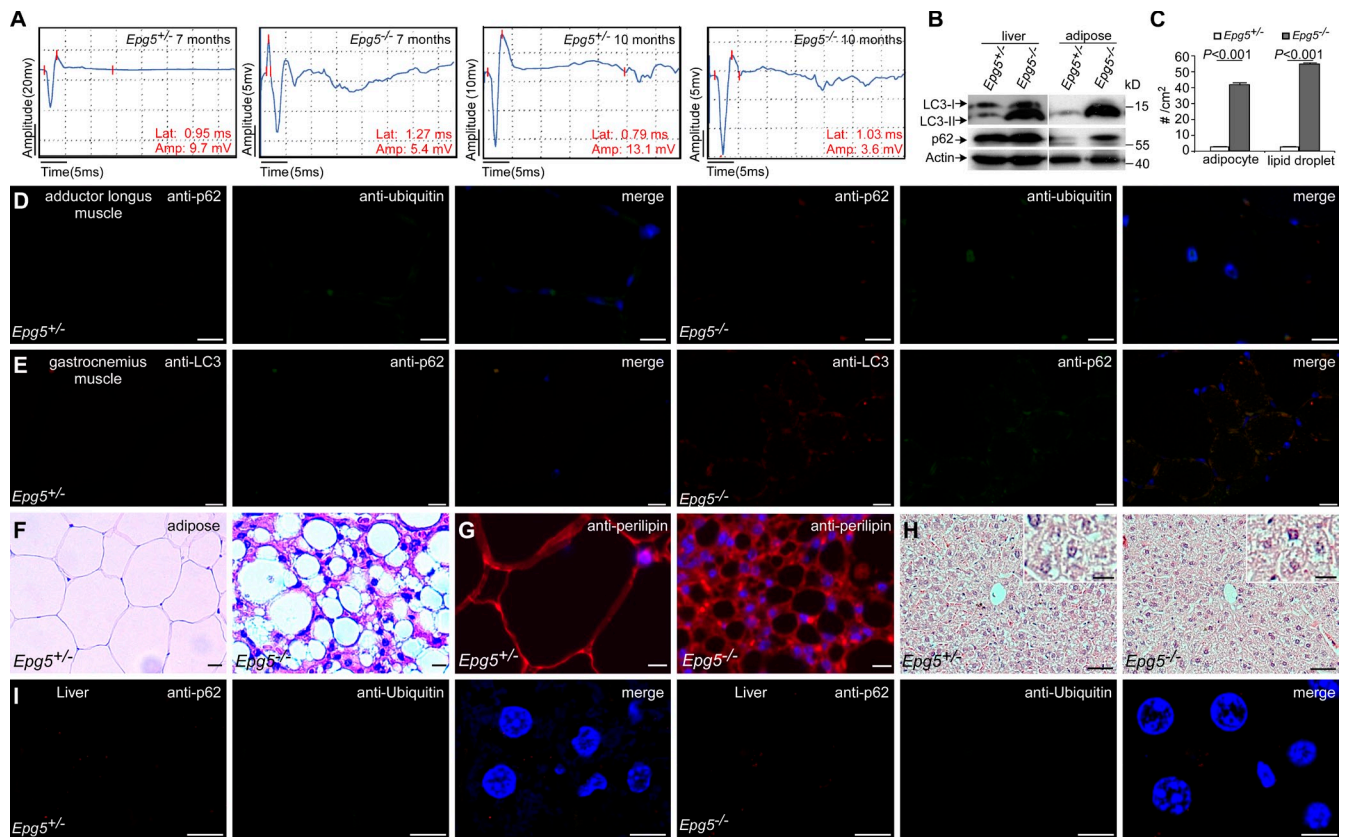


Figure S2. Muscle atrophy in *Epg5*-deficient mice. (A) CMAP of the gastrocnemius muscle elicited by distal stimulation of the sciatic nerve in *Epg5*^{-/-} mice at the age of 7 and 10 mo exhibited increased latency (Lat) and decreased amplitude (Amp). The left, middle, and right red lines indicate the start, peak, and end of an action potential, respectively. (B) Total liver and adipose proteins from *Epg5*^{+/-} and *Epg5*^{-/-} mice were extracted, separated by SDS-PAGE, and analyzed by immunoblotting with anti-LC3 and anti-p62 antibodies. Results are representative of at least three experiments. (C) The numbers of adipocytes and lipid droplets in control and *Epg5* knockout mice at 11 mo of age. Means ± SEM of four mice are shown. (D) Double immunostaining with anti-p62 (red) and antiubiquitin (green) aggregates reveals that no evident p62 aggregates or ubiquitin-positive inclusions accumulate in the adductor longus muscles of *Epg5*^{-/-} mice. (E) Coimmunostaining reveals the colocalization of LC3 (red) and p62 (green) in gastrocnemius muscles from *Epg5*^{-/-} but not *Epg5*^{+/-} mice. (F) H&E staining of gonadal white adipose tissue from *Epg5*^{+/-} and *Epg5*^{-/-} mice at 11 mo of age shows reduced adipocyte size and increased lipid droplet number in knockout mice. (G) Immunostaining with the antiperilipin antibody, which labels the membrane of the lipid droplet, also shows that *Epg5* knockout adipocytes are multilocular. (H) H&E staining of liver tissue shows no histological change in *Epg5*^{-/-} mice at 11 mo of age. Higher magnification views are shown in the insets. (I) Coimmunostaining of p62 (red) and ubiquitin (green) in livers from *Epg5*^{-/-} and *Epg5*^{+/-} mice indicates no p62 or ubiquitin accumulation in mutant mice. Bars: (D, E, G, H [insets], and I) 10 μm; (F) 20 μm; (H, main images) 50 μm.

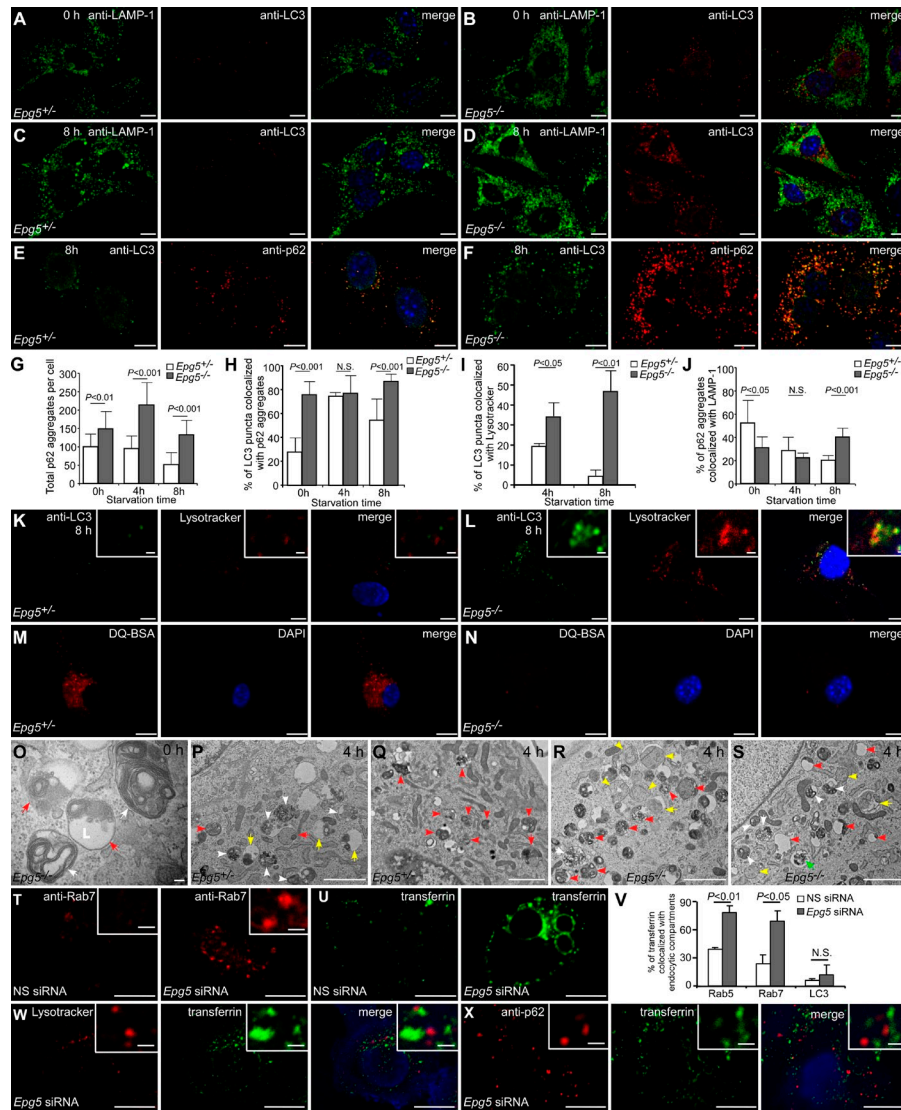


Figure S3. *Epg5*^{-/-} MEFs show a defect in the maturation of autophagosomes into degradative autolysosomes. (A–D) Fusion of autophagosomes, stained by anti-LC3 (red), and lysosomes, stained by anti-LAMP-1 (green), in *Epg5*^{-/-} and *Epg5*^{+/+} MEFs. *Epg5*^{-/-} and *Epg5*^{+/+} MEFs were starved for the indicated time and then stained by anti-LC3 and anti-LAMP-1 antibodies. (E and F) Colocalization of LC3 puncta with p62 aggregates in *Epg5*^{-/-} MEFs. Cells were starved for the indicated time and then stained by anti-LC3 and anti-p62 antibodies. (G) Mean number of p62 aggregates in *Epg5*^{+/+} and *Epg5*^{-/-} MEFs that were starved for the indicated time. (H) Percentage of LC3 puncta colocalized with p62 aggregates in *Epg5*^{+/+} and *Epg5*^{-/-} MEFs that were starved for the indicated time. (I) Colocalization ratio of LC3 and LysoTracker-stained acidic lysosomes in control and *Epg5*^{-/-} MEFs 4 and 8 h after starvation. (J) Percentage of p62 aggregates colocalized with LAMP-1-labeled structures in *Epg5*^{+/+} and *Epg5*^{-/-} MEFs that were starved for the indicated time. (K and L) Distribution of LC3 puncta and LysoTracker-stained acidic lysosomes (red) in *Epg5*^{+/+} and *Epg5*^{-/-} MEFs. (M and N) Autolysosomes stained with DQ-BSA in *Epg5*^{+/+} and *Epg5*^{-/-} MEFs. Accumulation of fluorescent signal, generated from lysosomal proteolysis of DQ-BSA, is much lower in *Epg5*^{-/-} MEFs. (O) EM images of autophagic vacuoles in unstarved *Epg5*^{-/-} MEFs. The red arrows indicate late autolysosomes. The white arrows show multilayered membranes probably derived from secondary structures assembled from previously deconstructed membranes. An area with a lipid-like appearance is indicated (L). (P and Q) After 4-h starvation, *Epg5*^{+/+} MEFs contain many autophagic vacuoles. (P) Numerous autophagic vacuoles at various stages of the autophagic process including an autophagosome (red arrow), an early autolysosome (aAV-I with recognizable content, red arrowhead), and late autolysosomes (aAV-II with unrecognizable disintegrated structures, white arrowheads). The autophagosome indicated by the red arrow has just fused with an aAV-II vacuole (white arrowhead). Late-stage lipid-containing vacuoles with dense residual material (aAV-III) can also be seen (yellow arrows). (Q) The red arrow indicates a complex autophagic vacuole with material at various stages of degradation (early and late aAV-II stage) inside it. The arrowheads indicate aAV-IIs. (R and S) Dramatic accumulation of autophagic elements at various stages of autophagic flux in *Epg5*^{-/-} MEFs after starvation. (R) The white arrow shows an aAV-I containing recognizable rough ER cisterns and ribosomes. The red arrowheads indicate aAV-IIs. The red arrow shows a complex vacuole composed of a morphologically intact part (on the left) and an aAV-II-type part with identifiable swollen ribosomes. The yellow arrowheads and arrows show autophagosomes. The yellow arrows point to autophagosomes with a cleft between two separate membranes. (S) The white arrow shows an aAV-I stage autophagic vacuole with recognizable rough ER cisterns. The yellow arrow indicates an autophagosome with the typical cleft between the two layers of the double membrane. The yellow arrowheads point to autophagosomes. The green arrow indicates an aAV-I with swollen ribosomes. The white arrowheads show aAV-IIs. The red arrowheads point to aAV-III vacuoles. (T) Immunostaining with the anti-Rab7 antibody shows enlarged late endosomes in *Epg5* siRNA-treated cells. (U) *Epg5* knockdown causes abnormal enlarged vacuoles whose surface is labeled by transferrin, indicating that the vacuoles are derived from defective endocytic recycling. (V) Colocalization of transferrin with different endosomal compartments in control and *Epg5* siRNA-treated cells. The transferrin puncta in *Epg5* siRNA-treated cells are separable from LC3 punctate structures. (W and X) LysoTracker staining or immunostaining with p62 antibodies was performed in *Epg5* siRNA-treated cells that were incubated with fluorescently labeled transferrin. Transferrin did not colocalize with LysoTracker-stained acidic lysosomes (W) or p62 aggregates (X). Higher magnification views are shown in the insets. Error bars indicate SEMs. Bars: (A–F, K–N, T, U, W, and X, main images) 10 μ m; (K [insets], L [insets], and P–S) 2 μ m; (O) 100 μ m; (T, W, and X, insets) 1 μ m.